Chapter 11

Jets and Missing Transverse Energy

The huge QCD cross section (Fig. 11.1) ensures that jets will dominate high-p_{T} physics at the LHC. Jets will not only provide a benchmark for understanding the detector, but will also serve as an important tool in the search for physics beyond the standard model. Event signatures for SUSY, Higgs boson production, compositeness, and other new physics processes require accurate reconstruction and measurement of jets coming from high-p_{T} quarks and gluons [205, 206, 207, 208]. The problems with associating a jet measured in a calorimeter with a scattered parton is an old, persistent problem in hadron collisions [209, 210, 211, 212]-[213, 214]. Jet energy resolution and linearity are key factors in separating signal events from backgrounds. Missing transverse energy resolution, which historically has played an important role in the W-boson discovery and the search for new phenomena at hadron colliders, is closely related to the calorimeter jet energy reponse.

A detailed description the calorimeter response, including pulse shape, digitization and zero suppression have been simulated with high statistics. Monte Carlo samples of fully simulated events at the detector level have been used to study jet and missing transverse energy response. The calibration procedures described in Chap. 5 together with these simulations provide an expectation of what we may expect for jet and missing transverse energy performance at startup. The commissioning phase of the detector will have a tremendous impact on understanding the calorimeter reponse and will help to refine plans for data-driven calibrations and jet energy scale determination.

11.1 Tower Definition and Thresholds

Readout cells in HCAL are arranged in a tower pattern in the η, φ space, projective to the nominal interaction point. The cells in the barrel region have the segmentation of 0.087×0.087, becoming progressively larger in the endcap and forward regions. Calorimeter towers (ECAL plus HCAL) are formed by addition of signals in η, φ bins corresponding to individual the HCAL cells. In total there are 4176 such towers, which when unfolded, may be represented in a familar "lego" plot (Fig. 11.2).

The towers are used as input to several standard jet clustering algorithms. The energy associated with a tower is calculated as the sum of all contributing readout cells which pass the online zero-suppression threshold and any additional offline software thresholds. For the purpose of jet clustering, the towers are treated as massless particles, with the energy given by the tower energy, and the direction defined by the nominal interaction point and the center of the tower.

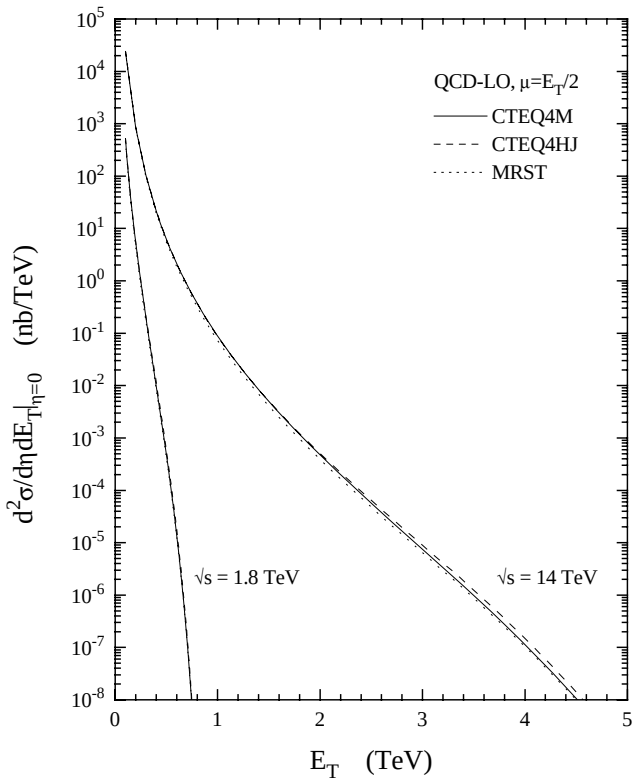

Figure 11.1: Inclusive jet cross section *vs.* jet transverse energy at the LHC compared with the Tevatron [215]. The cross section is seven orders of magnitude greater at the LHC than at the Tevatron kinematic limit, and the luminosity will also be more than two orders of magnitude greater.

Optimum performance of higher-level objects reconstructed from calorimeter towers requires careful selection of such inputs because calorimeter noise fluctuations can have significant impact on the reconstruction of low-p_T jets. Various schemes of suppressing contributions of noise to jet energies have been studied in detail. These studies include variation of thresholds on the the towers as well as the individual cells that define towers in both energy and E_{T}, Theshold studies were based on simulation of calorimeter response as implemented in ORCA 8.7.1. Energy distributions in HCAL cells show discrete ADC readout patterns (Fig. 5.12), with one ADC count corresponding to approximately 250 MeV in HB and HO, and 400 MeV HE. This quantization must be taken into account when setting thresholds.

The noise from towers in a simple cone of size $R = \sqrt{\eta^2 + \varphi^2}$ was invesitgated using several different sets of thresholds. These included three standard schemes in which: 1) no additional thresholds were applied (beyond online zero suppression), 2) a transverse energy cut $E_{\mathrm{T}} > 0.5$ GeV was applied to all towers, and 3) an energy cut $E > 0.8$ GeV was applied to all towers. Three additional schemes referred to as A, B, and C in Table 11.1 were designed to exclude one, two, and three ACD counts, respectively. The scheme A provides a significant reduction of noise in the $R = 0.5$ cone (from 8.5 GeV with no additional thresholds to 1.4 GeV), with only a 1 GeV loss of jet energy at $\eta = 0$. (For $\eta = 2$ the noise reduction goes from

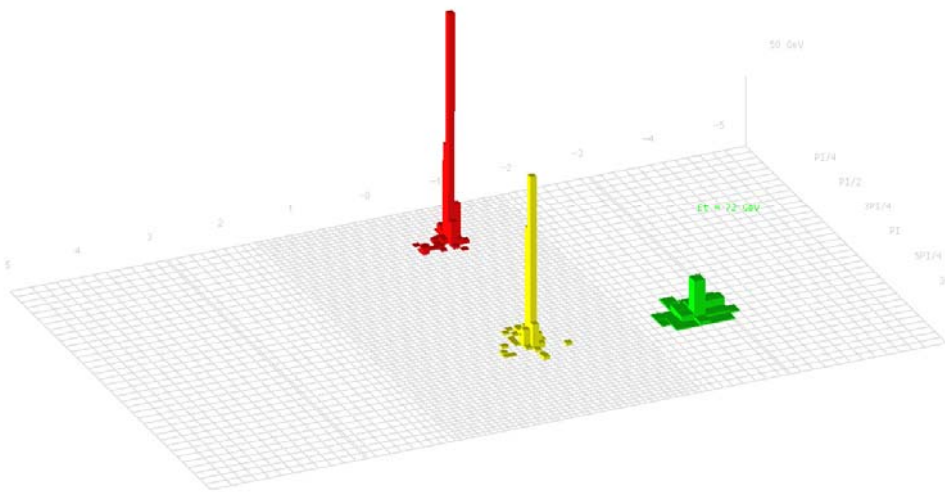

Figure 11.2: The η, φ segmentation of the CMS hadron calorimeter.

4.4 GeV to 1.1 GeV.)

Scheme	HB	HO	HE	EBSum	EESum
A	0.7	0.85	0.9	0.2	0.45
B	0.9	1.1	1.4	0.2	0.45
C	1.2	1.3	1.8	0.2	0.45

Table 11.1: Definitions of energy threshold schemes. Threshold values are given in GeV. EBSum (EESum) represent thresholds on the total EB (EE) energy in the tower (summed over all contributing crystals). All schemes are in addition to readout zero-suppression.

The corresponding jet efficiency curves *vs.* generated jet E_{T} for several different threshold schemes are shown in Fig. 11.3 a). The efficiency curves are remarkably similar in shape indicating that the corresponding jet resolutions for the different threshold schemes are very similar. Figure 11.3 b) shows the (uncorrected) raw jet E_{T} threshold needed to reconstruct jets with 50% efficiency as a function of MC generated jet E_T for different η regions.

11.2 Jet Algorithms

The first jet algorithms for hadron physics were simple cones [209],[216]. Over the last two decades, clustering techniques have greatly improved in sophistication. Three principal jet reconstruction algorithms have been coded and studied for CMS: the iterative cone [217], the midpoint cone [218] and the inclusive k_{T} jet algorithm [219, 220] The midpoint-cone and k_{T} algorithms are widely used in offline analysis in current hadron collider experiments, while the iterative cone algorithm is simpler and faster and commonly used for jet reconstruction in software-based trigger systems.

The jet algorithms may be used with one of two recombination schemes for adding the con-

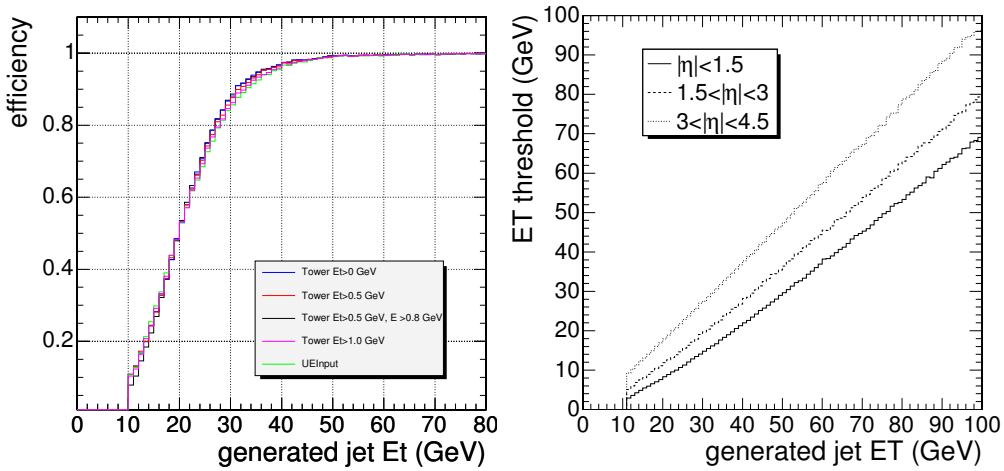

Figure 11.3: Left) Jet efficiency curves for several different threshold schemes. Right) Jet E_{T} threshold needed to reconstruct jets with 50% efficiency. **FIXME: relabel plots**

stituents. In the energy scheme, constituents are simply added as four vectors. This produces massive jets. In the E_{T} scheme, massless jets are produced by equating the jet transverse momentum to the the ΣE_{T} of the constituents and then fixing the direction of the jet in one of two ways: 1) $\sin\theta = \Sigma E_{\mathrm{T}}/E$ where E is the jet energy (usually used with cone algorithms), or 2) $\eta = \Sigma E_{\mathrm{T}i}\eta_i/\Sigma E_{\mathrm{T}}$ and $\phi = \Sigma E_{\mathrm{T}i}\phi_i/\Sigma E_{\mathrm{T}}$ (usually used with the k_{T} algorithm). In all cases the jet E_{T} is equal to $p_{\mathrm{T}}c$.

The inclusive k_{T} algorithm merges, in each iteration step, input objects into possible final jets and so the new jet quantities, the jet direction and energy, have to be calculated directly during the clustering. The cone jet algorithms, iterative and midpoint, group the input objects together as an intermediate stage and the final determination of the jet quantities (recombination) is done in one step at the end of the jet finding.

11.2.1 Iterative Cone

In the iterative cone algorithm, an E_{T}-ordered list of input objects (particles or calorimeter towers) is created. A cone of size R in η,ϕ space is cast around the input object having the largest transverse energy above a specified seed threshold. The objects inside the cone are used to calculate a *proto-jet* direction and energy using the E_{T} scheme. The computed direction is used to seed a new proto-jet. The procedure is repeated until the energy of the proto-jet changes by less than 1% between iterations and the direction of the proto-jet changes by $\Delta R < 0.01$. When a stable proto-jet is found, all objects in the proto-jet are removed from the list of input objects and the stable proto-jet is added to the list of jets. The whole procedure is repeated until the list contains no more objects with an E_{T} above the seed threshold. The cone size and the seed threshold are parameters of the algorithm. When the algorithm is terminated, a different recombination scheme may be applied to jet constituents to define the final jet kinematic properties.

11.2.2 Midpoint Cone

The midpont-cone algorithm was designed to facilitate the splitting and merging of jets. The midpoint-cone algorithm also uses an iterative procedure to find stable cones (proto-jets) starting from the cones around objects with an E_{T} above a seed threshold. Contrary to the iterative cone algorithm described above, no object is removed from the input list. This can result in overlapping proto-jets (a single input object may belong to several proto-jets). To ensure the collinear and infrared safety of the algorithm, a second iteration of the list of stable jets is done. For every pair of proto-jets that are closer than the cone diameter, a *midpoint* is calculated as the direction of the combined momentum. These midpoints are then used as additional seeds to find more proto-jets. When all proto-jets are found, the splitting and merging procedure is applied, starting with the highest E_{T} proto-jet. If the proto-jet does not share objects with other proto-jets, it is defined as a jet and removed from the proto-jet list. Otherwise, the transverse energy shared with the highest E_{T} neighbor proto-jet is compared to the total transverse energy of this neighbor proto-jet. If the fraction is greater than f (typically 50%) the proto-jets are merged, otherwise the shared objects are individually assigned to the proto-jet that is closest in η,ϕ space. The procedure is repeated, again always starting with the highest E_{T} proto-jet, until no proto-jets are left. This algorithm implements the energy scheme to calculate the proto-jet properties but a different recombination scheme may be used for the final jet. The parameters of the algorithm include a seed threshold, a cone radius, a threshold f on the shared energy fraction for jet merging, and also a maximum number of proto-jets that are used to calculate midpoints.

11.2.3 Inclusive k_{T} Algorithm

The inclusive k_{T} jet algorithm is a cluster-based jet algorithm. The cluster procedure starts with a list of input objects, stable particles or calorimeter cells. For each object i and each pair (i, j) the following distances are calculated:

$$\begin{aligned} d_i &= (E_{\mathrm{T},i})^2 R^2, \\ d_{ij} &= min\{E^2_{\mathrm{T},i}\,,\, E^2_{\mathrm{T},j}\} R^2_{ij} \quad \text{with} \quad R^2_{ij} = (\eta_i - \eta_j)^2 + (\phi_i - \phi_j)^2, \end{aligned}$$

where R^2 is a dimensionless parameter normally set to unity [218]. The algorithm searches for the smallest d_i or d_{ij}. If a value of type d_{ij} is the smallest, the corresponding objects i and j are removed from the list of input objects. They are merged using one of the recombination schemes listed below and filled as one new object into the list of input objects. If a distance of type d_i is the smallest, then the corresponding object i is removed from the list of input objects and filled into the list of final jets. The procedure is repeated until all objects are included in jets. The algorithm successively merges objects which have a distance $R_{ij} < R$. It follows that $R_{ij} > R$ for all final jets i and j.

11.3 Jet Resolution

The jet resolution was determined from a sample of QCD dijet events with $0 < \hat{\mathrm{p}}_{\mathrm{T}} < \mathrm{GeV}/c$ were generated with PYTHIA 6.226, fully simulated with OSCAR 245, digitized and reconstructed assuming low luminosity conditions ($\mathcal{L} = 2 \times 10^{33}\mathrm{cm}^{-2}\mathrm{s}^{-1}$) [221]. This sample was split into 21 bins of $\hat{p}_{\mathrm{T}}$ with a statistics of 10k events per $\hat{p}_{\mathrm{T}}$ bin. All jets reconstructed in these events are included in the resolution fits. For the purpose of evaluating the linearity of the

jet response, particle-level jets were reconstructed from all stable particles (excluding neutrinos and muons) using all three jet algorithms: the iterative cone algorithm with a cone size $R = 0.5$, the cluster-based k_{T} algorithm, and the midpoint-cone algorithm. The E_{T} recombination scheme was used. The particle-level jets are required to have $|\eta| < 5$, corresponding to the full η coverage of the calorimeters. A matching criteria based on the distance $R = 0.2$ in η, ϕ space was used to associate particle-level and reconstructed jets axes.

The reconstructed jet transverse energy ($E_{\mathrm{T}}^{\mathrm{Rec}}$) was compared to the MC generated transverse energy ($E_{\mathrm{T}}^{\mathrm{MC}}$). The distribution of $E_{\mathrm{T}}^{\mathrm{Rec}}/E_{\mathrm{T}}^{\mathrm{MC}}$ was fit to obtain the resolution as shown in Fig. 11.4. The lower value of $E_{\mathrm{T}}^{\mathrm{Rec}}$ compared to $E_{\mathrm{T}}^{\mathrm{MC}}$ is due in part to the fact that the ECAL is calibrated on photons, whereas a substantial amount of jet energy deposited in the ECAL arises from pions. For the lowest energy jets, the distribution of of $E_{\mathrm{T}}^{\mathrm{Rec}}/E_{\mathrm{T}}^{\mathrm{MC}}$ is asymetric and a fit is done in the vicinity of the peak position. The results of these fits provide an MC jet correction function that may be applied to reconstructed jets.

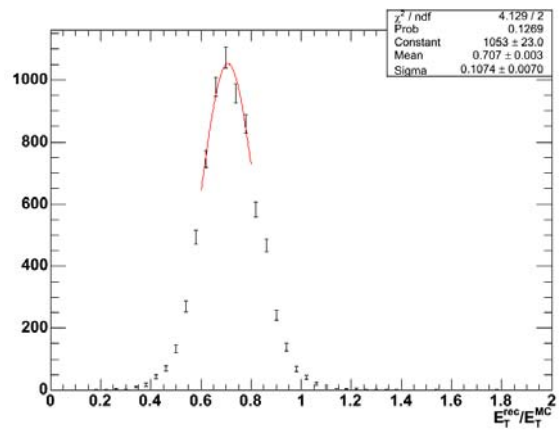

Figure 11.4: Distribution of reconstructed jet transverse energy ($E_{\mathrm{T}}^{\mathrm{rec}} = p_{\mathrm{T}}^{\mathrm{rec}}c$) divided by particle-level generated jet transverse energy ($E_{\mathrm{T}}^{\mathrm{MC}} = p_{\mathrm{T}}^{\mathrm{MC}}c$) for generated jets in the range $105\,\mathrm{GeV} < E_{\mathrm{T}}^{\mathrm{MC}} < 115\,\mathrm{GeV}$. The jets are reconstructed with the interative cone $R = 0.5$ algorithm.

The resolution plots were fitted with the following functional form:

$$\frac{\sigma(\frac{E_{\mathrm{T}}^{\mathrm{Rec}}}{E_{\mathrm{T}}^{\mathrm{MC}}})}{<\frac{E_{\mathrm{T}}^{\mathrm{Rec}}}{E_{\mathrm{T}}^{\mathrm{MC}}}>} = \frac{a}{E_{\mathrm{T}}^{\mathrm{MC}}} \oplus \frac{b}{\sqrt{E_{\mathrm{T}}^{\mathrm{MC}}}} \oplus c \tag{11.1}$$

where the first term is due to fixed energy fluctuations in the cone from electronics noise, pile-up and underlying event energy, the second term comes from the stochastic response of the calorimeter measurements and the last term is the constant term from residual non-uniformities and non-linearities in the detector response. The fits were done down to a transverse energies of 30 GeV in the barrel and endcap and 20 GeV in the forward region.

The resulting jet resolution for jets with $|\eta| < 1.4$ reconstructed with the iterative cone $R = 0.5$ algorithm is shown in Fig. 11.5. The resolution curves for the barrel, endcap and forward regions are shown in Fig. 11.6. The resolution curves on the measurement of ϕ and η of the jets for the barrel, endcap and very forward regions are shown in Figs. 11.7 and 11.8.

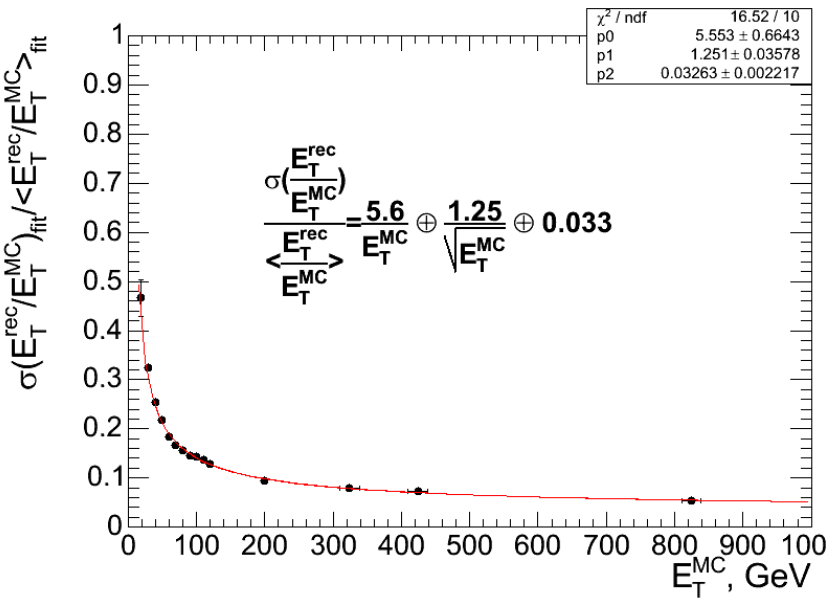

Figure 11.5: The jet transverse energy resolution as a function of the generated jet transverse energy for barrel jets ($|\eta|$ <1.4). The cuts E_{T} >0.5 GeV and E >0.8 GeV are used. The distance between generated and reconstructed jets is $\Delta R < 0.2$. The Monte Carlo jet calibration has been applied.

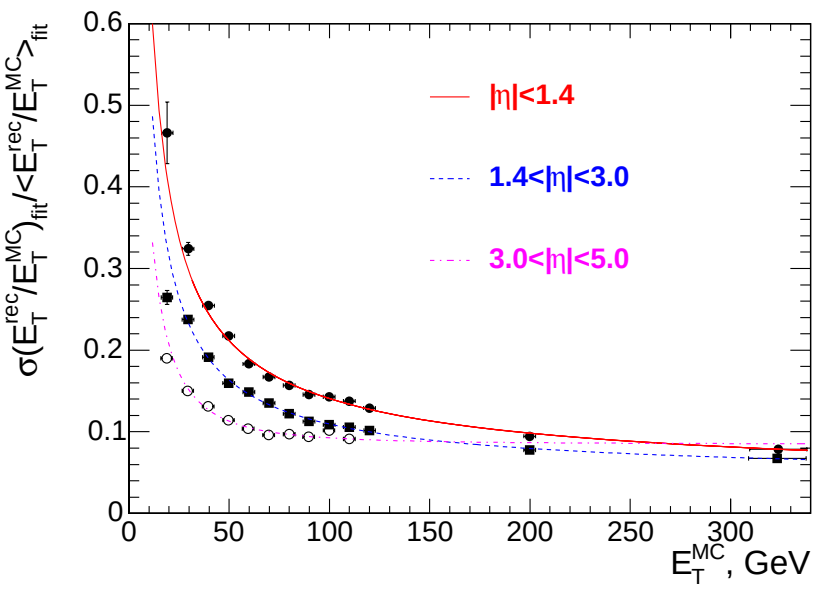

Figure 11.6: The jet transverse energy resolution as a function of the generated jet transverse energy for barrel jets ($|\eta|$ <1.4), endcap jets (1.4< $|\eta|$ <3.0) and very forward jets (3.0< $|\eta|$ <5.0). The jets are reconstructed with the interative cone $R = 0.5$ algorithm. The cuts E_{T} >0.5 GeV and E >0.8 GeV are used. The distance between generated and reconstructed jets is required to be $\Delta R < 0.2$. The Monte Carlo jet calibration has been applied.

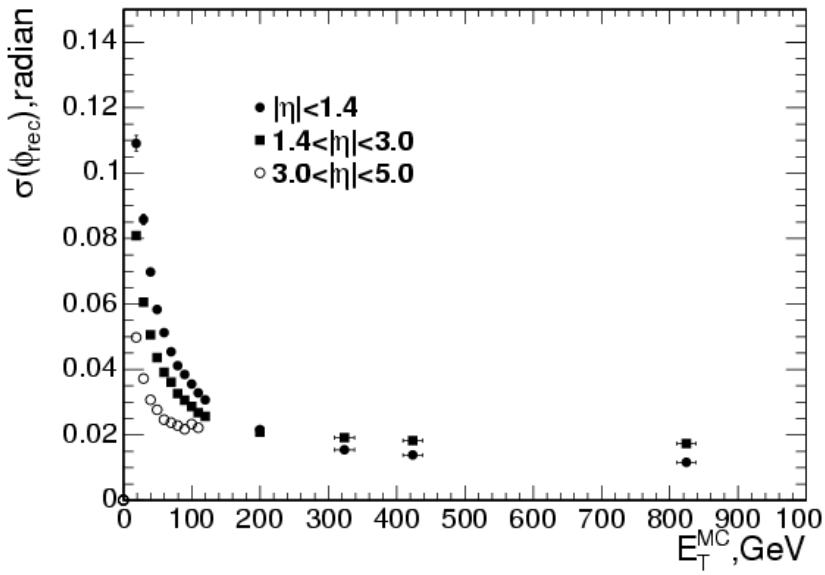

Figure 11.7: The jet ϕ angular resolution as a function of the generated jet transverse energy for barrel jets ($|\eta|$ <1.4), endcap jets (1.4< $|\eta|$ <3.0) and very forward jets (3.0< $|\eta|$ <5.0). The cuts E_{T} >0.5 GeV and E >0.8 GeV are used. The distance between generated and reconstructed jets is required to be $\Delta R < 0.2$.

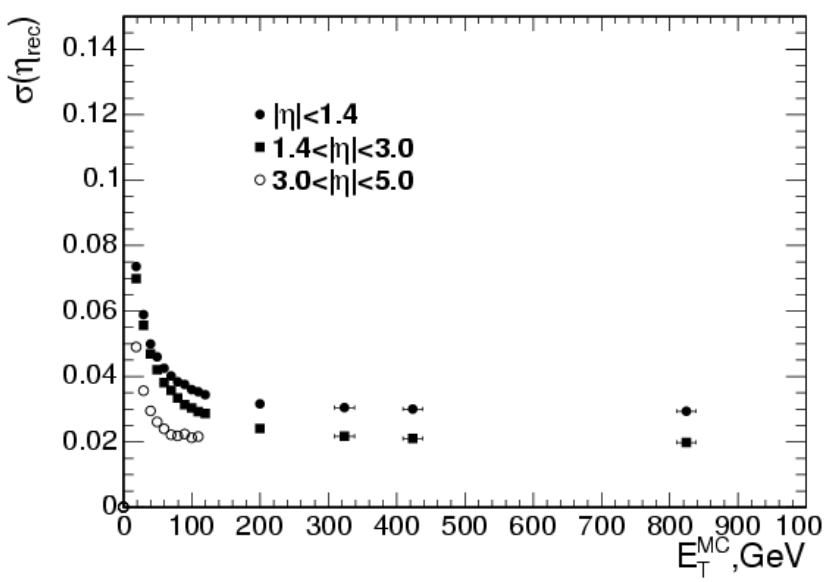

Figure 11.8: The jet η resolution as a function of the generated jet transverse energy for barrel jets ($|\eta|$ <1.4), endcap jets (1.4< $|\eta|$ <3.0) and very forward jets (3.0< $|\eta|$ <5.0). The cuts E_{T} >0.5 GeV and E >0.8 GeV are used. The distance between generated and reconstructed jets is required to be $\Delta R < 0.2$.

11.4 Missing Transverse Energy

Beginning with UA1 [222], all major detectors at hadron colliders have been designed to cover as much solid angle as practically possible with calorimetry [9]. The primary motivation of this is to provide as complete of a picture as possible of the event, including the presence of one or more energetic neutrinos or other weakly-interacting stable particles though apparent missing energy. Energetic particles produced in the direction of the beam pipe make it impossible to directly measure missing energy longitudinal to the beam direction, however, the transverse energy balance can be measured with an accuracy good enough to help establish a physics signature involving one or more non-interacting particles. The W boson was discovered and its mass determined to 3% with just 6 events due to the ability of UA1 to infer the presence of 40-GeV neutrinos with a resolution of a few GeV [223]. Since the time of the W discovery, measurement of missing transverse energy has been a major tool in the search for new phenomena at hadron colliders [224, 225, 226],[227].

Measurement of missing transverse energy vector ($\mathbf{E}_{\mathrm{T}}^{\mathrm{miss}}$) at the LHC will be complicated by the presence of pileup collisions. In CMS, measurement of $\mathbf{E}_{\mathrm{T}}^{\mathrm{miss}}$ will be further degraded by the photon/pion response of the ECAL and by the bending of tracks by the 4-T magnetic field. On the other hand, the excellent cell segmentation and good forward coverage of CMS will help measurement of $\mathbf{E}_{\mathrm{T}}^{\mathrm{miss}}$. In spite of all these detector subtleties, the $\mathbf{E}_{\mathrm{T}}^{\mathrm{miss}}$ resolution in CMS is expected to be dominated by combined ECAL plus HCAL calorimeter resolution as discussed in Section 11.3.

11.4.1 Comparison with UA1 and CDF

The missing transverse energy vector is calculated by summing individual calorimeter towers having energy E_n, polar angle θ_n and azimuthal angle ϕ_n:

$$\mathbf{E}_{\mathrm{T}}^{\mathrm{miss}} = \Sigma(E_n \sin\theta_n \cos\varphi_n \hat{\mathbf{i}} + E_n \sin\theta_n \sin\varphi_n \hat{\mathbf{j}}) = E_x^{\mathrm{miss}}\hat{\mathbf{i}} + E_y^{\mathrm{miss}}\hat{\mathbf{j}} \,.$$

Reconstructed muons are taken into account by replacing the expected calorimeter deposit (about 4 GeV) with the reconstructed track p_{T}. It was observed in UA1 that the $E_{\mathrm{T}}^{\mathrm{miss}}$ resolution was dependent on the overall activity of the event, characterized by the scalar sum of transverse energy in all calorimeter cells (ΣE_{T}). The resolution is observed to follow the form $\sigma = C\sqrt{\Sigma E_{\mathrm{T}}}\ \mathrm{GeV}^{1/2}$ where C is a constant that depends directly on the calorimeter jet resolution and ΣE_{T} is the scalar sum of the transverse energy of all calorimeter hits. For UA1, the calorimeter (jet) resolution was approximately $0.8\sqrt{E_{\mathrm{T}}}\ \mathrm{GeV}^{1/2}$ which let to an observed distribution of x- or y- components, E_x^{miss} or E_y^{miss}, in minimum bias events that was Gaussian with zero mean and standard deviation $\sigma_x = \sigma_y = 0.4\sqrt{\Sigma E_{\mathrm{T}}}\ \mathrm{GeV}^{1/2}$V [223]. The CDF experiment, which has a scintillating tile geometry similar to CMS (and a completely different magnetic field configuration compared to UA1, solenoid *vs.* dipole), observed $\sigma_x = 0.47\sqrt{\Sigma E_{\mathrm{T}}}\ \mathrm{GeV}^{1/2}$ in Run I [228]. From the UA1 and CDF results and the CMS jet resolution ($1.25\sqrt{E_{\mathrm{T}}}\ \mathrm{GeV}^{1/2}$) explained in Section 11.3, one may expect an $E_{\mathrm{T}}^{\mathrm{miss}}$ resolution in CMS of $\sigma_x \approx (0.6-0.7)\sqrt{\Sigma E_{\mathrm{T}}}\ \mathrm{GeV}^{1/2}$ for minimum bias events with no pileup, when dominated by the shower fluctuations and not electronic noise.

11.4.2 Resolution in Minimum Bias Events

Figure 11.9 shows the Monte Carlo distributions of ΣE_{T} and E_x^{miss} expected in CMS from a high statistics sample of fully reconstructed minimum bias events. In order to compare the CMS result to what may be expected from previous experiments, it is essential to separate out the stochastic part from the electronic noise, the latter of which can greatly effect the observed ΣE_{T}. For a given set of calorimeter thresholds, there corresponds an offset, *i.e.*, a minimum value of ΣE_{T} that will be recorded, which may be seen to be about 150 GeV in Fig. 11.9. The $E_{\mathrm{T}}^{\mathrm{miss}}$ resolution shown in Fig. 11.9 is 6.1 GeV in excellent agreement with expectations based on a stocahstic contribution of 4.8 GeV from calorimeter resolution and 3.8 GeV from electronic noise. It is important to note that at this stage, we are forming the vector $\mathbf{E}_{\mathrm{T}}^{\mathrm{miss}} = E_x\hat{\mathbf{i}} + E_y\hat{\mathbf{j}}$ using ECAL cells calibrated for photons and HCAL cells calibration for hadrons, appropriate perhaps for understanding the detector response to first collisions. It is believed that making use of energy flow techniques such as the charged track corrections described in Section 11.7 will ultimately improve the $\mathbf{E}_{\mathrm{T}}^{\mathrm{miss}}$ resolution.

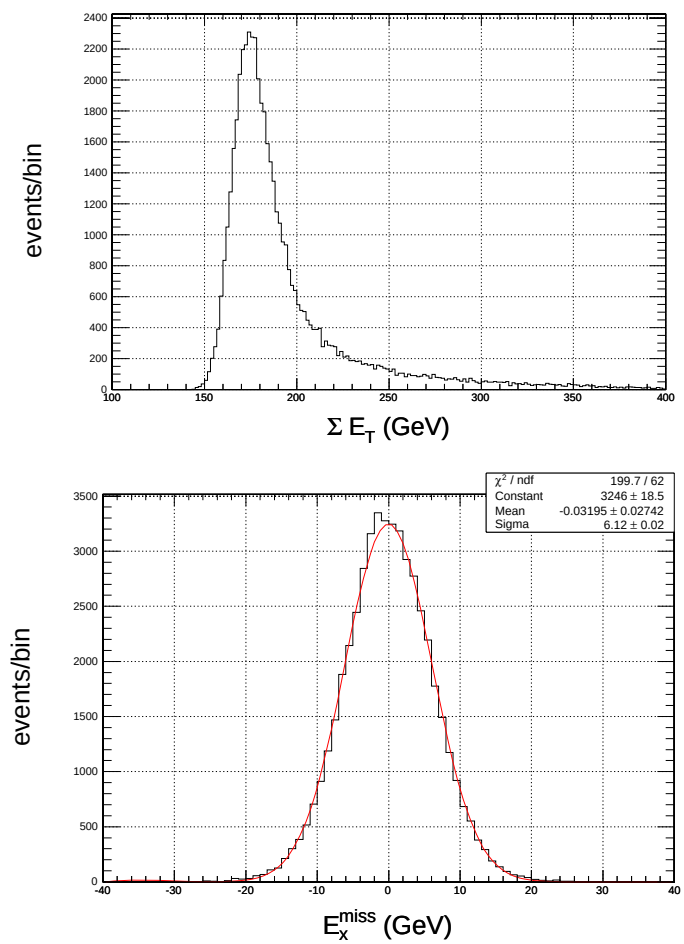

Figure 11.9: Top) Distribution of ΣE_{T} and Bottom) E_x^{miss} for minimum bias events with no pileup. The resolution is 6.1 GeV in agreement with expectations based on a stochastic term of $0.65\sqrt{\Sigma E_{\mathrm{T}}}\ \mathrm{GeV}^{1/2}$ and a noise contribution of 3.8 GeV.

11.4.3 Missing Transverse Energy Resolution in QCD Events

While the minimum bias events serve as a good check for understanding the calorimeters, a major background to any potential signal containing missing transverse energy will come from QCD. The observed $\mathbf{E}_{\mathrm{T}}^{\mathrm{miss}}$ resolution is degraded in the presence of event pileup which serves to increase the overall activity observed in the calorimeters. Even at low luminosity ($\mathcal{L} = 2 \times 10^{33}\mathrm{cm}^{-2}\mathrm{s}^{-1}$), there will be an average of 3.4 fully inelastic pileup events per 25 ns beam crossing, To study the detector $\mathbf{E}_{\mathrm{T}}^{\mathrm{miss}}$ resolution in events with hard collisions, 3×10^6 QCD events were generated and fully reconstructed. The events correspond to parton transverse momenta ($\hat{p}_{\mathrm{T}}$) ranging from 0-4000 GeV$/c$. The QCD events were all generated with low luminosity pileup.

The QCD events with the softest collisions, $0 < \hat{p}_{\mathrm{T}} < 15\mathrm{GeV}$, were used to make a connection with the resolution studies performed with the minimum bias sample. Figure 11.10 shows the observed ΣE_{T} and E_x^{miss} distributions in these soft QCD events. The observed missing transverse energy resolution of 9.9 GeV is comparable to that from minimum bias events with the addition of pileup.

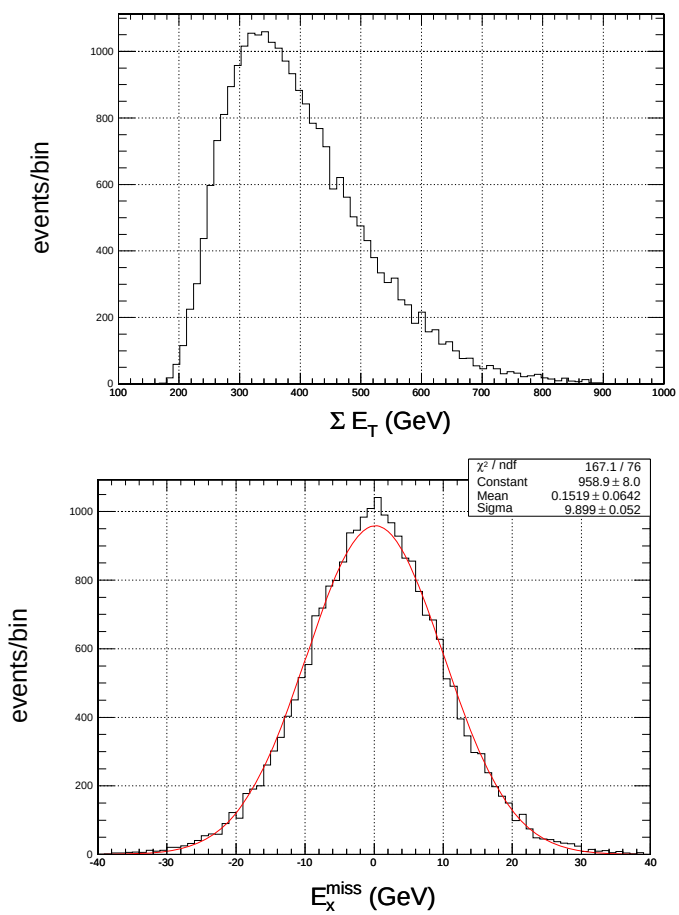

Figure 11.10: Top) Distribution of ΣE_{T} and Bottom) E_x^{miss} for soft QCD events ($0 < \hat{p}_{\mathrm{T}} < 15\mathrm{GeV}$) with pileup. The resolution is 9.9 GeV in agreement with expectations based the study with minimum bias events.

Figure 11.11 shows the reconstructed $E_{\mathrm{T}}^{\mathrm{miss}}$ resolution vs. observed ΣE_{T} for both minimum bias events (open circles) and soft QCD events having $0 < \hat{p}_{\mathrm{T}} < 15\mathrm{GeV}$ (squares). Low-luminosity pileup is included in both cases. In the region of overlap between the minimum bias and soft QCD samples (near ΣE_{T} = 250 GeV), the reconstructed transverse energy balance is in excellent agreement.

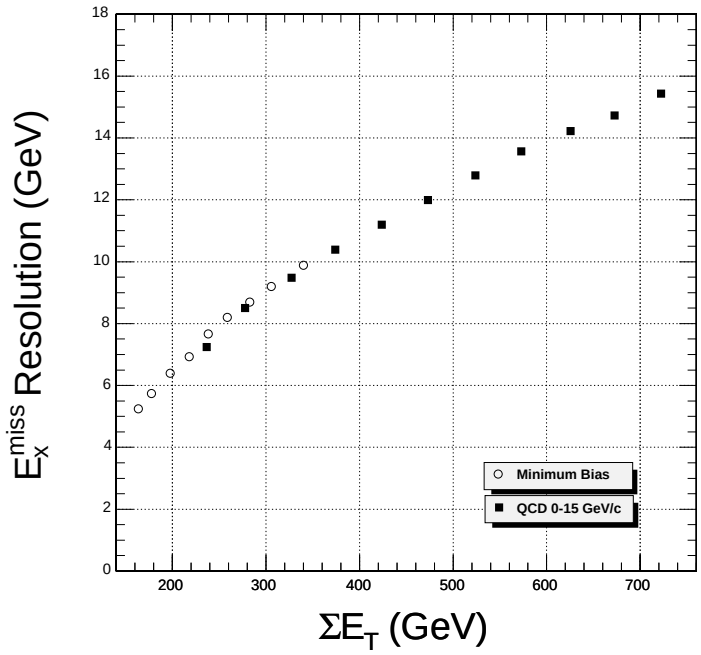

Figure 11.11: Missing transverse energy resolution *vs.* ΣE_{T} for QCD soft events, $0 < \hat{p}_{\mathrm{T}} < 15$ GeV, (squares) and minimum bias events (open circles). Low-luminosity pileup is included in both cases.

The reconstructed ΣE_{T} for QCD events is shown in Fig. 11.12. The value of ΣE_{T} is seen to range from about 500 GeV at $\hat{p}_{\mathrm{T}} \approx 65$ GeV to 1 TeV at $\hat{p}_{\mathrm{T}} \approx 340$ GeV to 1.7 TeV at $\hat{p}_{\mathrm{T}} \approx 700$ GeV. It is well known that $\mathbf{E}_{\mathrm{T}}^{\mathrm{miss}}$ resolution degrades in very active events compared to the ideal case of minimum bias events; for example, the average reconstructed missing transverse energy observed in UA1 jet events was $< E_{\mathrm{T}}^{\mathrm{miss}} >= 0.7\sqrt{\Sigma E_{\mathrm{T}}}$ GeV$^{1/2}$ [224] about 25% more than observed in minimum bias when scaled with ΣE_{T}. In hard-scatter QCD events, the distributions of E_x are also no longer perfectly Gaussian. In this case, the standard deviation of the E_x^{miss} distribution is used as the measure of resolution. Figure 11.13 shows the resolution for QCD events as a function of reconstructed ΣE_{T}. Note the agreement at ΣE_{T} = 500 GeV with Fig. 11.11 which gave $\sigma_x \approx 12$ GeV. The resolution at larger values of ΣE_{T}, however, follows a steeper path which approximately scales from the UA1 result. A fit to the resolution $(E_x^{\mathrm{miss}})^2 = (3.8\ \mathrm{GeV})^2 + (o.97\ \mathrm{GeV}^{1/2})^2 \Sigma E_{\mathrm{T}} + (0.012 \Sigma E_{\mathrm{T}})^2$.

The observed $E_{\mathrm{T}}^{\mathrm{miss}}$ balance is directly related to the $E_{\mathrm{T}}^{\mathrm{miss}}$ resolution. The observed $E_{\mathrm{T}}^{\mathrm{miss}}$ distribution, of course, by its construction has a one-sided tail. A small $\hat{p}_{\mathrm{T}}$ interval can create a wide spectrum of $E_{\mathrm{T}}^{\mathrm{miss}}$ at both generator and detector level. The reconstructed $E_{\mathrm{T}}^{\mathrm{miss}}$ for different intervals of parton-level generator $\hat{p}_{\mathrm{T}}$ are shown in Fig. 11.14. The reconstructed

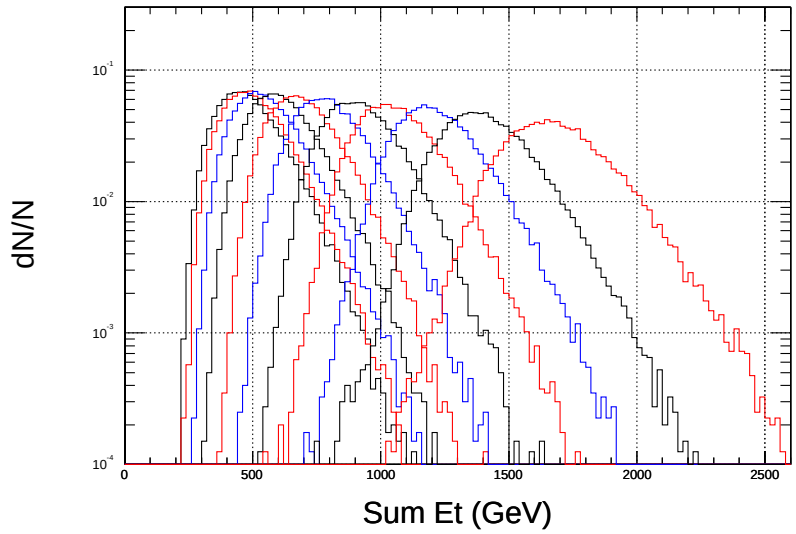

Figure 11.12: Distribution of ΣE_{T} observed in the detector for QCD events corresponding to $\hat{p}_{\mathrm{T}}$ ranges (from left to right) of 20-30, 30-50, 50-80, 80-120, 120-170, 170-230, 230-300, 300-380, 380-470, 470-600 and 600-800 GeV/c.

FIXME This plot needs to have labels fixed.

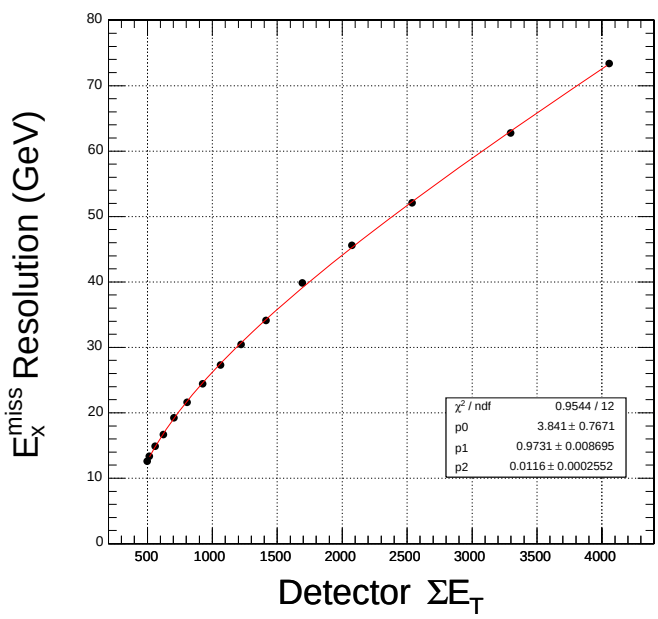

Figure 11.13: Missing transverse energy resolution *vs.* ΣE_{T} for QCD events with pileup. The fit gives a stochastic contribution of $0.97\sqrt{\Sigma E_{\mathrm{T}}}$.

$E_{\mathrm{T}}^{\mathrm{miss}}$ in QCD events (with pileup) is shown in Fig. 11.15. At ΣE_{T} = 1700 GeV, which corresponds to $p_{\mathrm{T}} \approx$ 700 GeV/c jets, an average $E_{\mathrm{T}}^{\mathrm{miss}}$ of about 50 GeV is observed. This number is consistent with measurement of such jets with a resolution of $1.25\ \mathrm{GeV}^{1/2}\sqrt{E_{\mathrm{T}}}$. A fit to the reconstructed missing transverse energy gives $(E_{\mathrm{T}}^{\mathrm{miss}})^2 = (5.4\ \mathrm{GeV})^2 + (1.23\ \mathrm{GeV}^{1/2})^2 \Sigma E_{\mathrm{T}} + (0.019 \Sigma E_{\mathrm{T}})^2$.

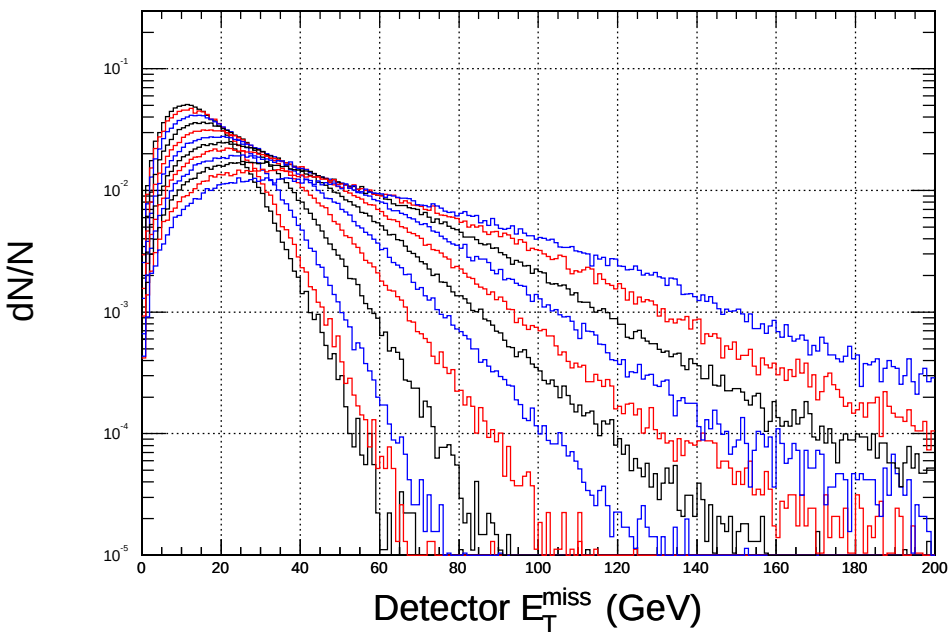

Figure 11.14: Missing transverse energy spectra in QCD samples that correspond to parton-level $\hat{p}_{\mathrm{T}}$ ranges of (from left to right) 20-30, 30-50, 50-80, 80-120, 120-170, 170-230, 230-300, 300-380, 380-470, 470-600, 600-800 and 800-1000 GeV/c.

As an additional check of detector $\mathbf{E}_{\mathrm{T}}^{\mathrm{miss}}$ performance, one may look at the resolution in a direction orthogonal to the jet axis. By choosing this direction, the observed resolution is independent of the reconstructed jet resolution, but rather is dominated by the underlying event and pileup activity. This distribution is shown in Fig. 11.16 *vs.* ΣE_{T}. Once again, as expected, the resolution is comparable to that observed in soft collisions (Fig. 11.10). It is believed that the jet calibration described in the following section will to serve as the basis for more sophisticated $\mathbf{E}_{\mathrm{T}}^{\mathrm{miss}}$ corrections and that ultimately energy flow techniques that account for calorimeter nonlinearities, magnetic field, and good charged particle resolution from the tracker can improve $\mathbf{E}_{\mathrm{T}}^{\mathrm{miss}}$ resolution.

11.4.4 Corrections to $\mathrm{E}_{\mathrm{T}}^{\mathrm{miss}}$

For QCD events, where reconstucted $\mathbf{E}_{\mathrm{T}}^{\mathrm{miss}}$ is an artifact of detector response, it is observed that correcting the jet energies (as described in the next section) does not significantly improve the missing transverse energy resolution except in the case where the leading jets have significantly different values η (and thus, much different energies). In events which have a large true $\mathbf{E}_{\mathrm{T}}^{\mathrm{miss}}$, its reconstruction is underestimated due to non-linearity of the calorimeter.

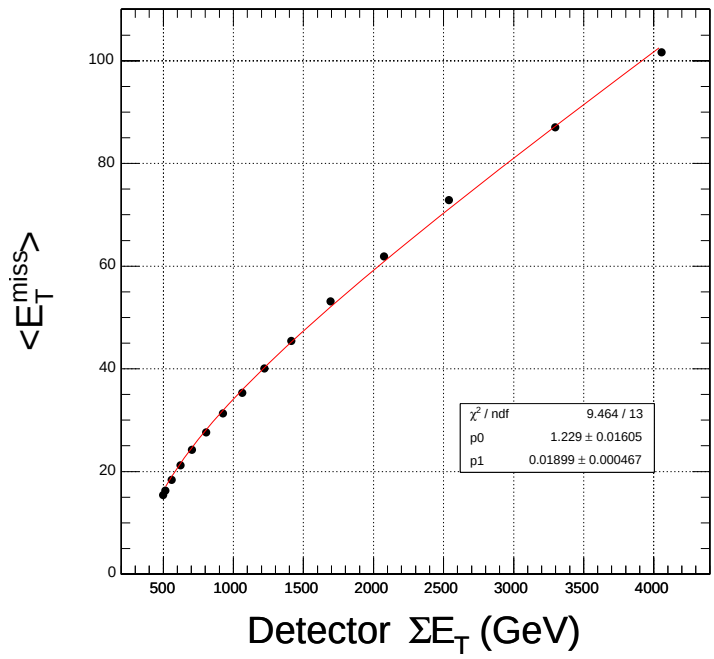

Figure 11.15: Average reconstructed $E_{\mathrm{T}}^{\mathrm{miss}}$ *vs.* ΣE_{T} for QCD events with pileup. The fit gives a stochastic contribution of $1.23\sqrt{\Sigma E_{\mathrm{T}}}$.

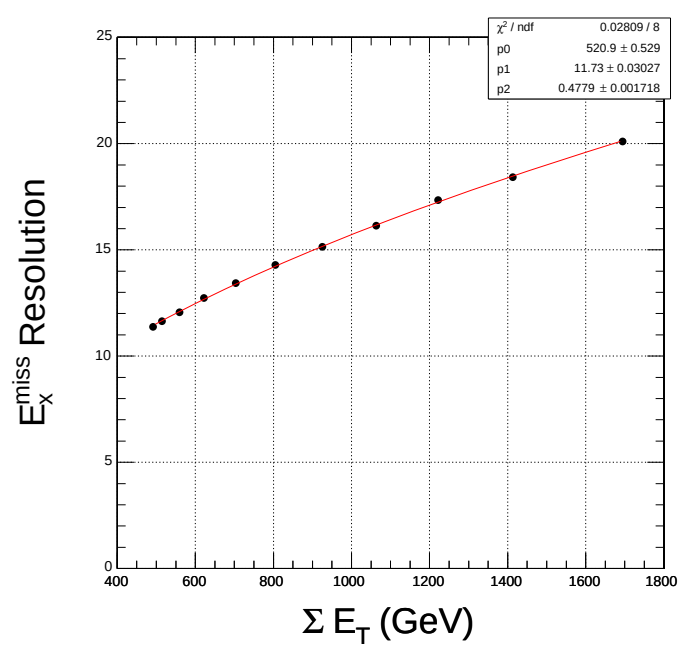

Figure 11.16: Missing transverse energy resolution in a direction orthogonal to the jet axis *vs.* ΣE_{T} of the entire event. The resolution is comparable to that observed in soft collisions.

In this case, a jet energy correction serves to help calibrate (linearize) the missing transverse energy scale.

A sample of $t\bar{t}$ events was used to investigate a number of corrections to measurement of $\mathbf{E}_{\mathrm{T}}^{\mathrm{miss}}$ in events with one or more energetic neutrinos (*i.e.*, genuine $\mathbf{E}_{\mathrm{T}}^{\mathrm{miss}}$). Figure 11.17 shows the resolution before and after jet corrections for inclusive $t\bar{t}$ events *vs.* reconstructed $E_{\mathrm{T}}^{\mathrm{miss}}$. For large values of reconstructed $E_{\mathrm{T}}^{\mathrm{miss}}$, we observe an improvement in resolution of nearly 15%.

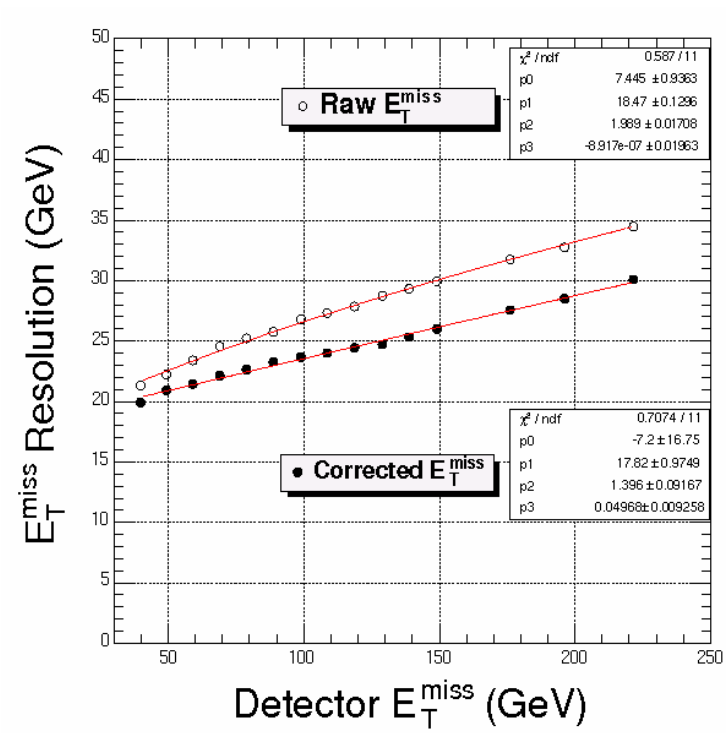

Figure 11.17: Missing transverse energy resolution before and after jet corrections for inclusive $t\bar{t}$ events *vs.* reconstructed ΣE_{T}.

Figure 11.17 shows the error in the reconstructed missing transverse energy scale before and after jet corrections for inclusive $t\bar{t}$ events *vs.* reconstructed reconstructed $E_{\mathrm{T}}^{\mathrm{miss}}$. As anticipated, the jet corections (by design) also bring back the true missing transverse energy scale by correcting for calorimeter particle response.

11.4.5 Angular Resolution

Figure 11.19 shows the angular resolution (φ) of the reconstructed missing transverse energy direction from inclusive $t\bar{t}$ events as a function of reconstructed $E_{\mathrm{T}}^{\mathrm{miss}}$, before and after the corrections described in Section 11.4.4. One may see that for low values of $E_{\mathrm{T}}^{\mathrm{miss}}$, the angular resolution is comparable to jet size, while for larger values of $E_{\mathrm{T}}^{\mathrm{miss}}$ the angular resolution approaches that of the calorimeter tower size.

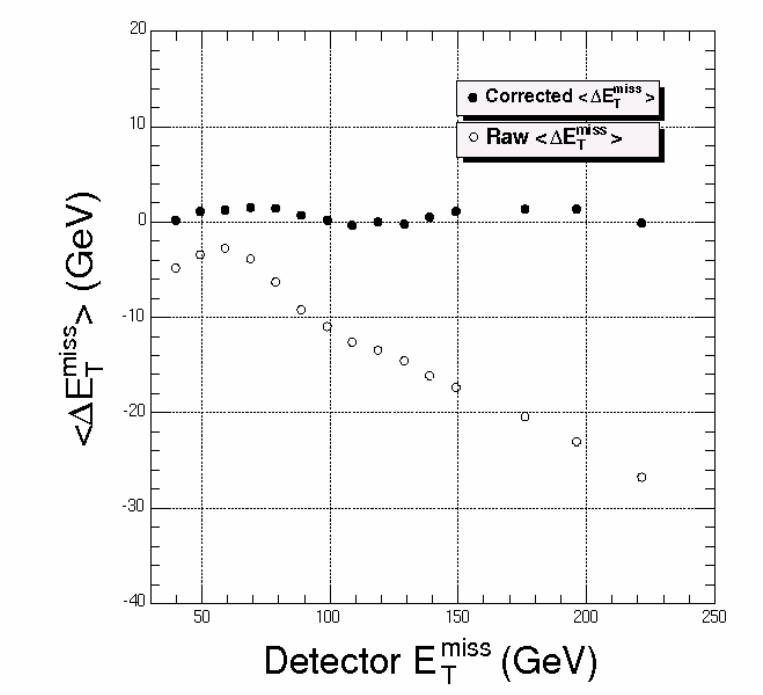

Figure 11.18: Error in the reconstructed missing transverse energy scale before and after jet corrections for inclusive $t\bar{t}$ events *vs.* reconstructed $E_{\mathrm{T}}^{\mathrm{miss}}$.

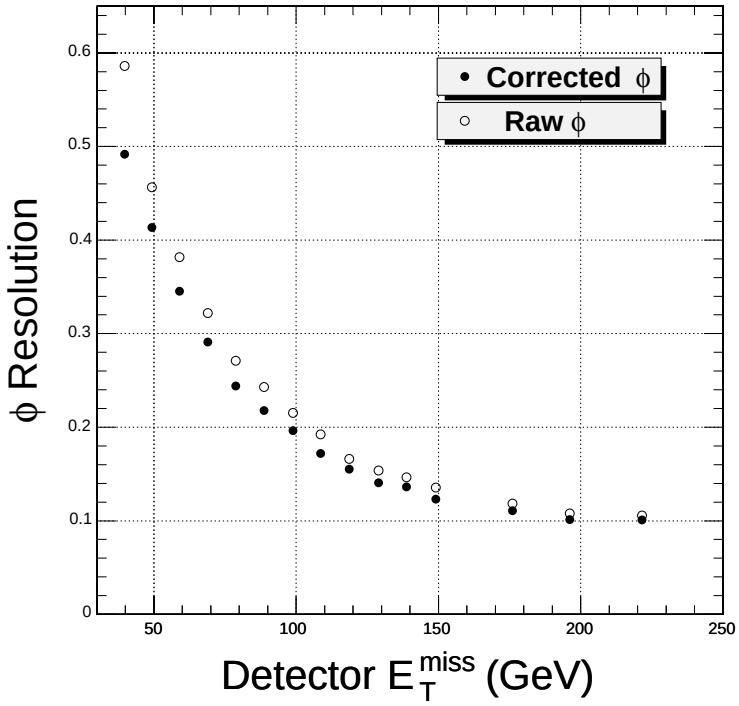

Figure 11.19: Error in the direction of the vector $\mathbf{E}_{\mathrm{T}}^{\mathrm{miss}}$ das a function of reconstructed $E_{\mathrm{T}}^{\mathrm{miss}}$ in inclusive $t\bar{t}$ events before and after corrections.

11.5 Jet Calibration

Jet calibration takes place in two steps: 1) a reconstructed jet is corrected to particle-level and 2) the particle-level jet is corrected to parton level, depending on the parton type assumed in the analysis. The particle-level calibration provides a corrected energy scale for particles entering the calorimeter towers grouped together by the jet algorithm. The parton-level calibration corrects the energy of a particle-level corrected jet to the energy of the parton that originated the jet.

There are two components to the particle-level calibration: offset and response. The offset correction results from multiple interactions in the same bunch crossing (in-time pileup), pileup from interactions from neighboring bunch crossings, electonic noise, and the underlying event. The response correction is due to the difference between measured total energy and the true particle total energy. Note: the resonse correction usually includes a correction for energy not collected by the jet algorithm due to shower spreading into (or out of) neighboring towers, but originating from particles in (or out of) the jet.

A set of calibrations need to be derived for each jet algorithm, set of algorithm parameters, and any other cuts (such as electromagentic fraction or number of tracks). The jet calibration provides an average correction for jets reconstructed under a particular configuration. Similarly, the parton-level correction is also tied to the specifics of how the jets were reconstructed and selected. Some corrections, such as p_{T} and η dependences, are parameterized directly in the calibration procedure and cuts on these quantities do not affect the average jet calibration.

11.5.1 Data-Driven Calibration Strategy

The MC calibration techinique described in Section 11.3 together with the radioactive source calibration and test beam measurements will provide a starting point understanding the initial calorimeter calibration. The data, however, will provide a number of invaluable tools which may be used to facilitate the overall calibration procedure [229]. The first stage of the calibration will check the radioactive source calibration at the tower level, while the second stage will check the calibration of tower clusters.

The following procedures have been identified for verfiying the calorimeter tower calibration:

- Measure noise with beam-crossing triggers to check and adjust thresholds.
- Take data without zero-suppression to study the offset in clusters of calorimeter towers.
- Check and adjust phi symmetry with minimum bias triggers.
- Use isolated muons from W decays to compare the tower-to-tower response to radioactive source source measurements and test beam muons.
- Compare isolated high p_{T} charged tracks with test beam data,

The following procedures will be used to calorimeter cluster (jet) calibration: processes.

- Measure the effect of pile-up on clustering algorithms and thresholds.
- Use p_{T} balance in QCD dijet events as described in Section **??** to calibrate the jet energy scale *vs.* η and verify the resolution.

- Use p_{T} balance in γ+jet events as described in Section **??** to calibrate the absolute energy scale.
- Use W mass fitting in tagged $\mathrm{t\bar{t}}$ events as described in Section **??** to check and fine tune the jet energy scale.

It is believed that a 5% overall uncertainty in the jet energy scale may be achieved at this stage.

11.5.2 Dijet Balancing

Transverse momentum balance in QCD dijet events is a proven technique to measure relative jet response and resolution from data. The results can be used to calibrate and test the full CMS simulation.

Events are selected having one of the two leading jets in the region $|\eta| < 1$ (the "barrel" jet). The other leading jet (the "probe" jet) may be at any value of η. The dijet p_{T} is defined by

$$p_{\mathrm{T}}^{\mathrm{dijet}} = (p_{\mathrm{T}}^{\mathrm{probe}} + p_{\mathrm{T}}^{\mathrm{barrel}})/2,$$

We divide the data into bins of probe jet η and measure the dijet balance (b) defined by

$$b = (p_{\mathrm{T}}^{\mathrm{probe}} - p_{\mathrm{T}}^{\mathrm{barrel}})/p_{\mathrm{T}}^{\mathrm{dijet}}$$

The dijet relative response, defined as the fractional difference between the jet response in the probe region and the jet response for $|\eta| < 1$, is then $2\bar{b}/(2-\bar{b})$, where $\bar{b}$ is the mean value of the dijet balance distribution. The dijet relative response as a function of probe jet η is shown in Fig. 11.20. A significant η dependence is expected due to tower geometry and other instrumental effects, however, the distribution flattens when MC corrections are applied.

Dijet balancing can be used to derive calibrations as a function of η based solely on the data. The errors shown on the response in Fig. 11.20 correspond to a QCD sample of approximately 10^4 events. If an efficient trigger can be deployed for a p_{T} threshold of 120 GeV/c prescaled to an HLT rate of 2.5 Hz, calibration measurements with the precision shown in Fig. 11.20 may be made from one hour of data taking. One day of data taking would be enough to calibrate the relative response of the detector to jets with a statistical error of 0.5% in the barrel and 2% in the endcap. These data could be further used to monitor the stability of jet response versus η, and provide daily calibrations to HLT triggers that require stable and uniform jet response.

The jet resolution can be measured from the RMS (σ_B) of the dijet balance. Each of the two leading jets contributes to the RMS, so the single jet resolution is given by $\sigma_B/\sqrt{2}$. Hard QCD radiation, generally manifested as extra jets in the event, broadens the resolution and creates non-Gaussian tails. We reduce the effects of QCD radiation to negligible levels by selecting events in which there are not any additional jets with $p_{\mathrm{T}} > 0.1 p_{\mathrm{T}}^{\mathrm{dijet}}$. To measure the jet resolution in the barrel we require that both of the leading jets have $|\eta| < 1$. Fig. 11.21 shows the barrel jet resolution measured with dijet balancing as a function of dijet p_{T}, which is comparable for both reconstructed jets and corrected jets. The statistics on the measured resolution are what can be expected for 10^5 events in the indicated dijet p_{T} range.

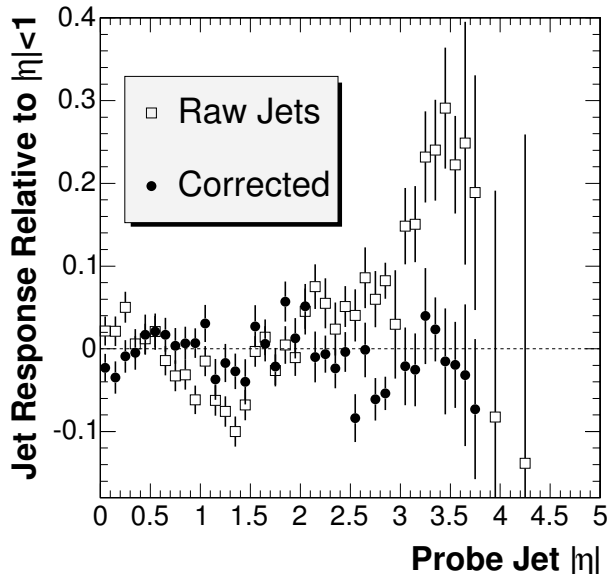

Figure 11.20: Jet response as a function of $|\eta|$ for $120\ \mathrm{GeV}/c$ <dijet $p_{\mathrm{T}} < 250\ \mathrm{GeV}/c$. The graphs compares raw jets (open boxes) with corrected jets (solid circles). The indicated level of precision may be obtained on one hour of data taking.

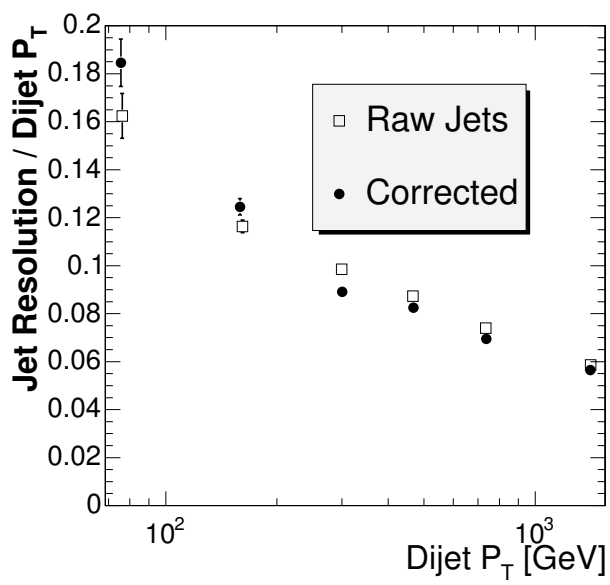

Figure 11.21: Jet resolution for $|\eta| < 1$ as a function of dijet p_{T}.

11.5.3 γ+Jet Events

Apart from higher-order initial-state effects, the direct photon produced from Compton ($qg \rightarrow q + \gamma$) and annihilation ($q\bar{q} \rightarrow g + \gamma$) processes has a transverse momentum that is balanced by the jet. The high resolution ($\sim$1%) of the electromagnetic calorimeter provides an accurate measurement of the photons and is the basis of the jet calibration procedure. The primary complications of this calibration procedure come from initial-state radiative corrections and a background of QCD dijet events where one jet is misidentified as a photon in the calorimeter [230].

The measured observable $k_{\rm jet} \equiv p_{\rm T}^{jet}/p_{\rm T}^{\gamma}$ provides an approximate value for the true parton-level calibration of the jet given by $k_{\rm jet}^{\rm true} \equiv p_{\rm T}^{jet}/p_{\rm T}^{\rm parton}$. The calibration constant given by $k_{\rm jet}^{\rm true}$ is the inverse of the correction factor needed to convert the measured transverse momentum of the jet to the transverse momentum of an initial parton. In the presence of initial state radition, the transverse momentum balance of the photon and the parton is broken, leading to a two-dimensional distribution in $p_{\rm T}^{\rm parton}$ and $p_{\rm T}^{\gamma}$ (Fig.11.22a). The correlation is symmetric along the line $p_{\rm T}^{\gamma} = p_{\rm T}^{\rm parton}$. Thus the $p_{\rm T}^{\gamma} - P_{\rm T}^{\rm parton}$ balance is preserved by statistically averaging over events with a fixed sum in the transverse momentum of the photon and the parton.

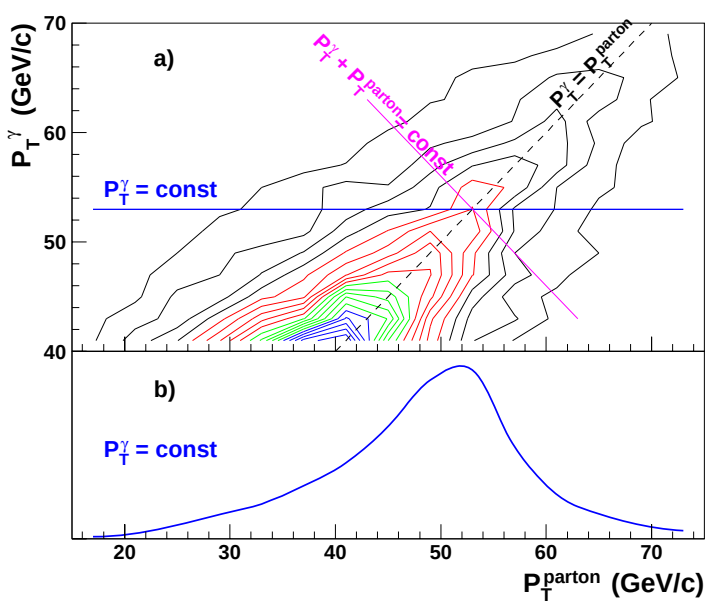

Figure 11.22: a) Distribution of the 2D correlation between the photon and parton transverse momenta, and b) the parton transverse momentum spectrum for a fixed photon transverse momentum in events with direct photons.

Calibration coefficients are determined directly in bins of $p_{\rm T}^{\gamma}$, however, the $p_{\rm T}$ balance of the γ+parton system is broken in this case. From Fig.11.22b, projecting a slice of the $p_{\rm T}^{\rm parton}$ distribution for $p_{\rm T}^{\gamma}$ =constant shows a strongly asymmetric distribution with $\langle p_{\rm T}^{\rm parton} \rangle < p_{\rm T}^{\gamma}$. For the measurement of the transverse momentum of the parton, the value $k_{\rm jet}$ will contain

an error from initial state radiation corresponding to $\Delta = k_{\rm jet} - k_{\rm jet}^{\rm true} = p_{\rm T}^{\rm parton}/p_{\rm T}^{\gamma} - 1$. This error is significant (6.3% for $p_{\rm T}^{\gamma} = 100$ GeV), but may be essentially eliminated by defining calibration coeficients $k_{\rm jet}$ to correspond to the peak of the $p_{\rm T}^{\rm jet}/p_{\rm T}^{\gamma}$ spectrum.

Fully simulated γ+jet events are generated with low luminosity ($\mathcal{L} = 2 \times 10^{33}{\rm cm}^{-2}{\rm s}^{-1}$) and reconstructed using the iterative cone and cluster-based K_T-algorithms. Quantum chromodynamics dijet events in which one jet is misidentified as photon provide the main background to the calibration sample.

The selection of events at the detector level was done with tight cuts on photon isolation ($E_{T\,\gamma}^{isol} < 5$ GeV), the angle between the photon and the jet ($\Delta\phi_{\gamma,\rm jet} > 172°$) and on transverse energy of additional jets in event ($E_T^{\rm jet2} < 20$ GeV). As a measure of the photon isolation, the value of $E_{T\,\gamma}^{\rm isol}$ is defined to be the scalar sum of the transverse energy in calorimeter cells within a cone of radius $R = 0.7$ in η, ϕ space with repect to the direction of the parton and outside a central array of 7×7 crystals in the electromagnetic calorimeter. The sum was computed for cells above a threshold of 0.36 and 1.8 GeV for the barrel and endcap of the electromagnetic calorimeters, respectively, and above 2 GeV for the hadron calorimeter. A cut on $E_{T\,\gamma}^{\rm isol}$ defined in this way gave a large background suppression while maintaining reasonably high signal efficiency(approximately 50%). Figure 11.23 shows signal to background ratio as a function of photon transverse energy. For $E_T^{\gamma} > 150$ GeV the background is suppressed well below the signal level, while for $E_T^{\gamma} < 40$ GeV, the background dominates the signal.

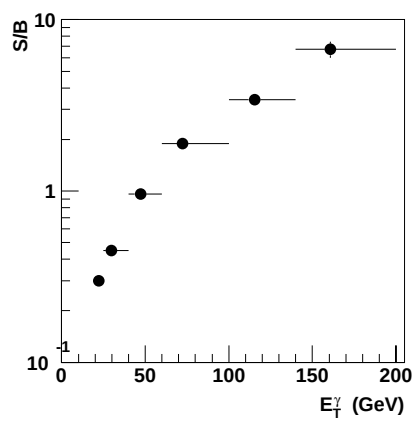

Figure 11.23: The ratio of signal to background after event selection cuts $E_{T\,\gamma}^{isol} < 5$ GeV, $\Delta\phi_{\gamma,\rm jet} > 172°$, and $E_T^{\rm jet2} < 20$ GeV.

Figure 11.24 shiws the predicted values are presented for the calibration coefficients and their true values for quark jets and QCD jets, using the iterative cone jet algorithm ($R = 0.5$) and a threshold cut on the transverse energy of calorimeter towers, $E_{\rm T} > 0.5$ GeV. Depending on the algorithm, algorithm parameters and calorimeter cell thresholds, there is a corresponding steepness to the $E_{\rm T}$ dependence of the calibration coefficients and a spread of their values for quark and gluon jets. A strong $E_{\rm T}$ dependence and large spread in response contributes to the error on the calibration.

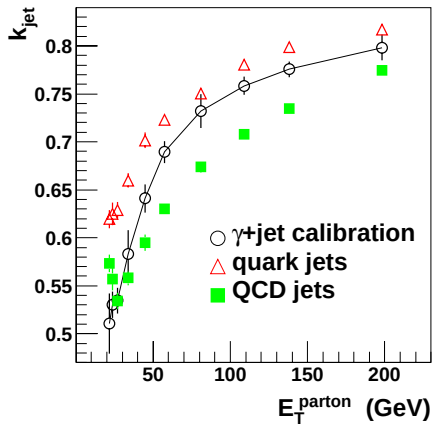

Figure 11.24: The predicted values of calibration coefficients (circles) and their true values for quark (triangles), QCD jet (squares) for the iterative cone algorithm for $|\eta_{\rm jet}| < 1.5$.

Figure 11.25illustrates the sensitivity of calibration errors to the choice of jet algorithm. Quark jets are less sensitive to the jet algorithm compared to gluon jets. For QCD jets, the $k_{\rm T}$ clustering algorithm produces smaller errors than the interative cone. It should be noted that the range of errors on the jet calibration coefficients do not characterize the quality of jet algorithm. Comparing the effect of thresholds on the calorimeter cell readings, it is found that the lower thresholds yield the most uniform calibration coefficents.

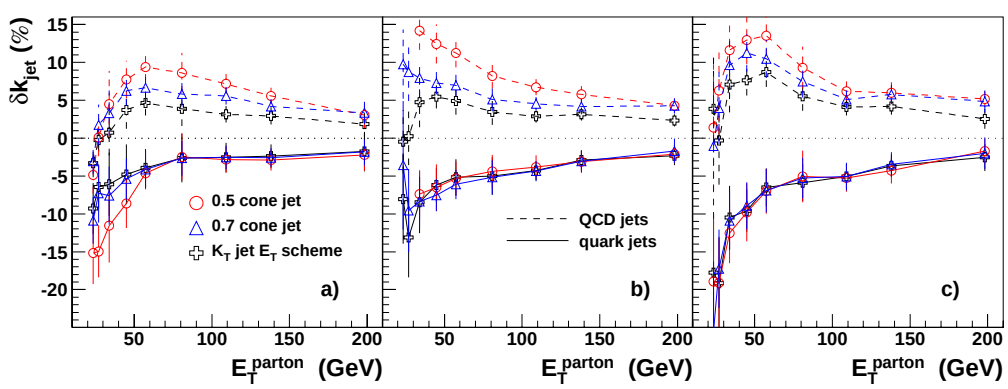

Figure 11.25: Relative systematic errors on the calibration of quark (solid lines) and QCD jets (dashed lines) for the iterative cone algorithm with cone radii of $R = 0.5$ (circles) and $R = 0.7$ (triangles) and for the $k_{\rm T}$-cluster algorithm using the $E_{\rm T}$ scheme (crosses) for the following thresholds on calorimeter cells: a) $E_T^{tower} > 0.5$ GeV, b) $E^{tower} > 1$ GeV, and c) $E^{tower} > 1.5$ GeV.

11.5.4 Parton-level Corrections

In the CDF experiment, it has been shown that total energy of particles in various cones in the vicinity of a parton is well simulated by PYTHIA, enabling the parton energy scale to be corrected to the particle-level jet energy scale via Monte Carlo derived correction factors ($k_{\rm ptcl} \equiv p_{\rm T}^{\rm jet}/p_{\rm T}^{\rm parton}$). Figure 11.26 shows these corrections are shown as a function of quark or gluon $p_{\rm T}$, For quark jets and a cone radius of $R = 0.7$, the correction to parton energy is insignificant. The η dependence of the parton corrections are shown in Fig. 11.27).

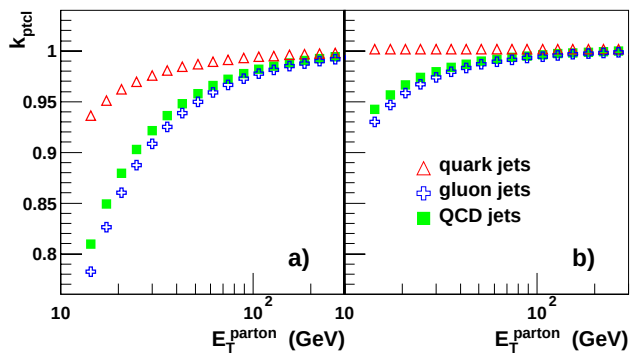

Figure 11.26: Ratio of transverse momenta of particle-level jets to the transverse momenta of the initial partons for QCD, quark and gluon jets collected in cones of (a) $R = 0.5$ and (b) $R = 0.7$ at $|\eta_{jet}| < 1.5$ as a function of transverse parton energy. These corrections are computed with PYTHIA 6.214.

The parton level corrections are different for light quark and gluon jets. The parton level correction for the mixture of quark and gluons (corresponding to QCD sample, for instance) can be obtained with expression

$$K_{q+gmixture} = \frac{f \times K_q + K_g}{f+1}, \tag{11.2}$$

where f is the ratio of the number of quarks and gluons in the dataset. The parton level correction for the any channel can be derived from the correction for quarks and gluons, supposing the relative ratio of quarks and gluons. The determination of the relative ratio of quarks and gluons in the data is expected to be difficult and would lead the additional systematic errors on the jet energy scale. The b-jet has the fragmentation different both from light quarks and gluons and, thus, requires the special set of the correction curves. The first estimation of the parton level corrections will be obtained from γ+jet and W$\rightarrow$ jet + jet (via $\bar{t}$) samples. in each of these samples, parton balance can be measured with reasonably high accuracy. In applying the calibration, however, one needs to take into account the differences

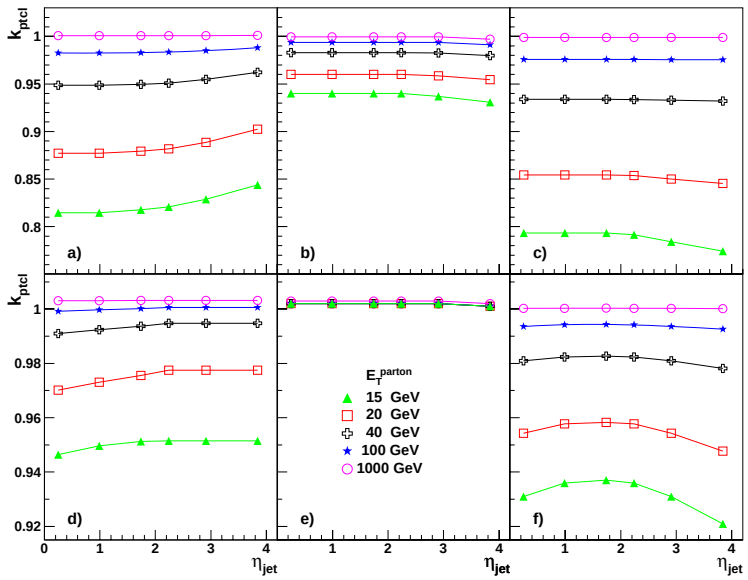

Figure 11.27: Ratio of transverse momenta of particle-level jets to the transverse momenta of the initial partons for QCD, quark and gluon jets collected in cones of (a) $R = 0.5$ and (b) $R = 0.7$ as a function of jet pseudorapidity for the different energies of parton. These corrections are computed with PYTHIA 6.214.

between quark and gluon jets.

11.5.5 W boson Mass Constraint in Top Quark Events

The large cross section for $\mathrm{t\bar{t}}$ (800 pb) provides an unprecidented opportunity to calibrate quark jets from W-boson decay. Precise understanding of these jets will be an invaluable calibration tool as top is predicted to be the largest single source of background for most physics searches. A sample of 3×10^6 inclusive $\mathrm{t\bar{t}}$ events have been used for this study, corresponding to an integrated luminosity of 3.8 fb^{-1}. Top events are selected as having a high-p_{T} muon from one of the W decays, four (or more) jets and two b-tags.

Muons reconstructed and identified using the methods described in Chapter [**FIXME**]. A combined likelihood ratio of several observables is determined for each muon in the final state in order to enhance the purity of choosing the correct lepton from the leptonic W decay. The muon having the largest combined likelihood ratio value is taken as the hard lepton of interest. The muon is required to be within the tracker acceptance of $|\eta| < 2.4$ and have $p_{\mathrm{T}} > 20\ \mathrm{GeV}/c$.

Jets are reconstructed with the iterative cone algorithm ($R = 0.5$) with cone seeds selected from all calorimeter towers above a pseudo-rapidity dependent energy threshold determined from the average underlying event deposits. Events ar eselected with at least four jets with pseudo-rapidities in the range of the tracker or $|\eta| < 2.4$ and a raw or not calibrated

E_t above 10 GeV. The particles in the jets must have a flight direction through the tracker to allow for a proper performance of the b-tagging algorithm. An initial MC jet calibration has been applied as descussed in Section 11.3.

In order to discriminate between jets originating from the heavy b-quarks compared to the light quarks, a b-tag probability was constructed from the b-tag discriminant variable. A likelihood ratio which can be interpreted as a b-tag probability is constructed as

$$L^b(x) = \frac{P_b(x)}{P_b(x) + P_c(x) + P_{\text{others}}(x)} \tag{11.3}$$

where $P_i(x)$ are the probability density functions of quark flavour i in the dimension of the b-tag discriminant x. The event is required to have at least 4 jets in a range of 2mm around the primary vertex in the direction along the beamline with a `MCJet` calibrated E_t above 30 GeV. If more than four jets do fulfill this criterion, the four jets with the highest E_t are choosen to be those from the $\mathrm{t\bar{t}}$ process. Exactly two of these four jets need to have a b-tag probability L^b larger than 60%, the remaining two jets should not exceed a probability value of 30% . It is also required that the cones of these four jets do not overlap in η, ϕ space. The cuts above result in 3700 signal events and 940 background events per 1 fb^{-1}. The backgrond events arise mainly from other $\mathrm{t\bar{t}}$ decays.

The non-b-tag jets are identified as originating from the W boson decay, Figure 11.28 shows this dijet mass distribution. The W mass can be fit with a simple Gaussian function with the mean value m_W. taken as an estimate of the reconstructed W boson mass. The estimated W boson mass from this fit is larger than the known value of 80.4 GeV/c^2. This was to be expected, in part, because the MC jet calibration applied was determined using a QCD sample dominated by gluon jets.

The W mass is then reconstructed after correcting the jets with a relative calibration shift ΔC (in %) on their energy scale. The direction of the jet is invariant for this procedure, while the magnitude of its momentum is rescaled in order to keep the mass of the jet invariant. The value of ΔC is found which gives the best W mass fit. The resulting value of ΔC is theestimate of the energy scale correction needed for jets originating from light flavoured partons. From this technique, a value of ΔC = -14.5 $\pm$ 0.3 % is obtained.

A possible bias in the ΔC estimator must be studied carefully. From the selected signal events, one can identify the light quark jets which match perfectly to the Monte Carlo simulated parton. using an angular matching $\Delta R < 0.2$ in η, ϕ space. The reconstructed energy (E_{jet}) can be compared to the generated parton energy E_{gen}. The average value of $1 - (E_{\text{rec}}/E_{\text{gen}})$ can be taken as the true energy scale correction to be estimated, noted as ΔC_{true}. This value is found to be ΔC_{true} = -14.8% . The bias can therefore be estimated as $\Delta C_{\text{bias}} = \Delta C - \Delta C_{\text{true}}$ = -0.3 $\pm$ 0.3 % .

As the proposed measurement of the absolute jet energy scale wil not be limited by its statistical accuracy, the systematical uncertainties on the estimator are crucial. The influence of systematic effects on the estimation of m_W via the Gaussian fit on the spectrum can be translated into a systematic uncertainty on the estimation of ΔC.

The influence of pile-up is found to be ΔC(PU-noPU) = -3.1% . This was estimated by using simulated signal event samples with and without low luminosity pile-up collisions. This is the average effect on the energy scale on each reconstructed jet from the inclusion of pile-up

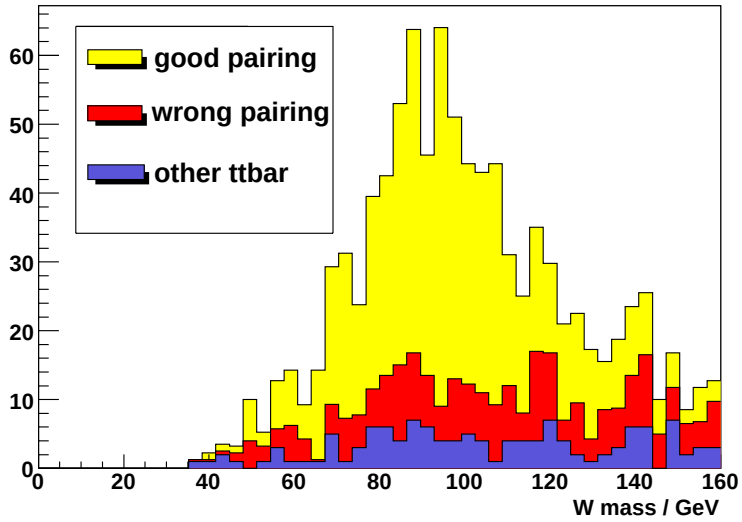

Figure 11.28: Distribution of the W boson mass spectrum. The combinatorial and process backgrounds are shown normalized to the integrated luminosity of the signal sample.

collisions in-time with the bunch crossing containing the hard-Q^2 event. With the invent of efficient pile-up subtraction methods, this difference should decrease.

The influence of the combinatorial background is estimated from a W boson mass spectrum with and without including this combinatorial background. The difference is found to be ΔC(Bck-noBck) = 0.13%. Systematics arising from the applied b-tagging algorithm are difficult to estimate and rely on their performance quality. These systematic influences from b-tagging will basically change the combinatorial and process background contribution and the effect is therefore more or less included in the systematic uncertainties described above. The total systematic uncertainty on ΔC is conservatively estimated to be equal to 3.1% and completely dominated by the effect of pile-up.

A similar method using both the W boson mass and the top quark mass constraints can be exploited to estimate the absolute jet energy scale of jets originating from b-quarks. On an event-by-event basis one can force the two light quark jets from the W decay to obtain the world average measured W boson mass. The energy scale of the b quark can then be adapted to fit the world average measured top quark mass.

11.6 Association of Jets With the Signal Vertex

One of the most experimentally challenging aspects of LHC physics is the issue of in time pileup, where minimum bias interactions can introduce additional jets into the event. A technique to efficiently associate jets with the signal vertex is needed to reduce the large luminosity-dependent instrumental background from pileup jets. The CMS tracker can provide this information by associating reconstructed charged tracks to primary vertices and

to jets. To associate a jet with a signal vertex, defined by a lepton or other high p_{T} tracks of interest, a significant fraction of the tracks in the jet should originate from this primary vertex.

Two approaches have been investigated to test whether jets originate from the signal vertex or not. They differ in the use of the calorimeter jet energy measurement.

- Method A:
  1) The variable α_{jet} is determined for each jet as the ratio of the sum of transverse momenta of all tracks found inside the jet cone and having the same vertex as the signal (by a z matching residual) to the transverse momentum of the jet as measured by the calorimeters, $\alpha_{jet} = \sum P_T^{track_\alpha} P_T^{jet}$.
  2) If $\alpha_{jet} > \alpha_0$, this jet is assigned to the signal vertex.
- Method B:
  1) The variable β_{jet} is determined for each jet as the ratio of the sum of transverse momenta of all tracks found inside the jet cone and having the same vertex as the signal to the transverse momentum of all tracks inside the jet cone, $\beta_{jet} = \sum P_T^{track_\alpha} P_T^{track}$.
  2) If $\beta_{jet} > \beta_0$, this jet is assigned to the signal vertex.

11.7 Jet Energy Correction Using Charged Tracks

It has been long ago demonstrated that precision charged particle tracking may be used to significantly enhance and linearize jet resolution [211, 212]. Energy flow techniques have been used successfully to improve jet measurement at HERA and LEP [231, 232]). Such corrections can become quite sophisticated and are expected to evolve as the detector becomes better understood.

A initial jet correction procedure has been identified for CMS [233, 234] which corrects for tracks swept out of the jet cone by 4-T magnetic field and replaces the expected calorimeter response for charged tracks with the corresponding energy detemined from a more accurate tracker momentum measurement. The expected calorimeter response for charged tracks is based on test beam measurements and Monte Crlo calculations. The procedure increases the jet energy due to an exchange of the underestimated response of calorimeters to charged hadrons with the momentum of the track in the tracker and adding the out-of-cone energy.

Samples of QCD dijet events in different were simulated with PYTHIA and digitized with no underlying event and no pile up scenario [234]. Jets are found at the generation and reconstruction levels using iterative cone algorithm with $R = 0.5$. A comparison is made of the reconstructed jet with the MC jet. The dependence of the resolution and the ratio on MC jet energy for jets generated with $|\eta| < 0.3$ are shown in Figs.11.29-11.30 for calorimetry and calorimetry-plus-tracker jets respectively. The linearity improves significantly with the track corrections. Approximately half of the resolution improvement results from recovering the of out-of-cone tracks.

To illustrate the expected improvement from using the track corrections, Z$'$ bosons ($m = 120\ \mathrm{GeV}/c^2$) decaying into light quarks were fully simulated and digitized with low-luminosity pileup. The Z$'$ mass was reconstructed from the two leading jets. Figure 11.31 shows the ratio of reconstructed to generated Z$'$ mass for with and without the track corrections. The

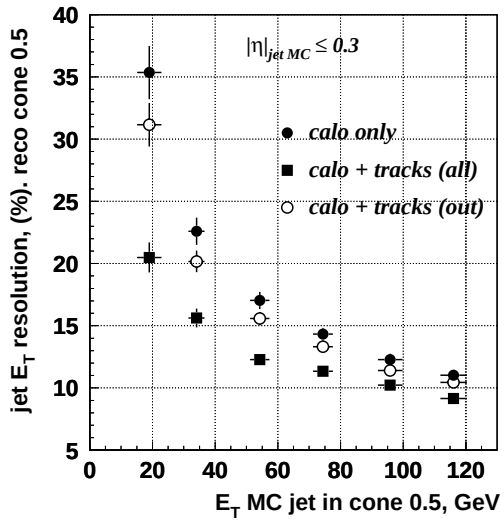

Figure 11.29: The jet E_{T} resolution as a function of generated jet E_{T} for reconstruction with calorimeter only (full circles), addition of out-of-cone tracks (open circles), and further charged track response corrections (full squares).

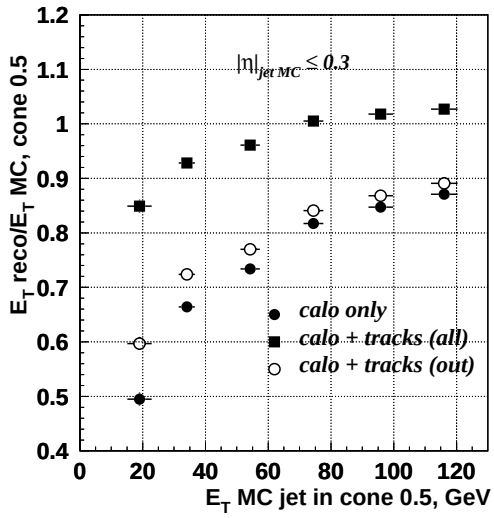

Figure 11.30: Ratio of reconstructed to generated jet E_{T} as a function of the generated jet E_{T} for reconstruction with calorimeter only (full circles), addition of out-of-cone tracks (open circles), and further charged track response corrections (full squares).

correct $Z^{'}$ dijet mass is obtained with use of the track corrections, with a systematical shift of about 1%, and the resolution is improved by about 10%.

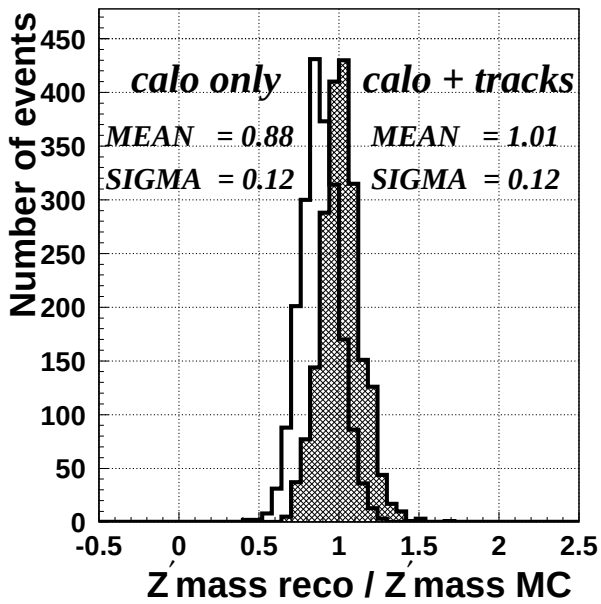

Figure 11.31: Ratio of the reconstructed to the generated Z′ mass with calorimeters only (empty histogram) and with track corrections (hatched histogram).

11.8 Jet Reconstruction in Heavy Ion Collisions

Jets from heavy ion collisions at the LHC may provide infomation about parton propagation through a quark-gluon plasma. The main challenge with jet reconstruction in heavy ion collisions is background arising from fluctuations of the transverse energy flow due to the large multiplicity of secondary particles in the event [235]. Predictions vary from 2000 to 8000 charged particles per unit of rapidity in central Pb–Pb collisions at the LHC.

The original jet finding algorithm was developed for reconstructing hard jets (E_T of order 100 GeV) in heavy ion collisions [**?**, **?**, **?**, **?**], where particles produced in a typical collision deposit transverse energy E_T up to 10 GeV in every calorimeter tower. The algorithm allows subtraction of the background energy due to the underlying event energy flow and identification of the hard jets on an event by event basis. In this study, jet finding is done with the background subtraction algorithm currently implemented in the CMS reconstruction software (ORCA).

11.8.1 Background Subtraction Algorithm

In heavy ion collisions at the LHC, jets are expected with trnasverse eneryg around 100 GeV. A jet finding algorithm has been developed to search for clusters above the average transverse energy flow.

- The average transverse energy of tower i ($\langle E_{\mathrm{T}}^{i} \rangle$) and its dispersion ($\sigma_i$) are calculated.
- All tower transverse energies are recalculated by subtracting the average tower

energy plus a factor k times its disersion (($E_{\mathrm{T}}^{i} - \langle E_{\mathrm{T}}^{i} \rangle - k\sigma_i$). If the value of the transverse tower energy after subtraction becomes negative, it is set to zero.

- Using the corrected tower energies, jets are found with the iterative cone algorithm.
- The average tower energies and dispersions are recalculated again using only towers outside of the jets. The original tower energies are used in this calculation.
- All tower energies are recalculated by subtracting the revised average tower energy plus k times its disersion. If the value of the transverse tower energy after subtraction becomes negative, it is set to zero.

A factor $k = 1$ is used in this study to compensate the positive bias in the reconstructed jet energy due to suppression of towers with the negative energy. This scheme gives an approximation for the reconstructed jet energy in Pb–Pb close to the energy obtained in pp.

11.8.2 Performance of Jet Reconstruction

Dijet events from pp collisions generated with PYTHIA are superimposed on 5.5 TeV Pb–Pb events which are generated with the HIJING Monte-Carlo generator using the default setting (quenching on) with $dN_{\mathrm{ch}}/dy|_{y=0} = 5000$. The combined events were fully digitized.

Jet reconstruction is studied using the background subtraction algorithm described above. The threshold on reconstructed jet energy is 30 GeV. Only the highest E_{T} jet in an event is used for futher analysis. The correlation between the reconstructed and generated jet E_{T} for Pb–Pb and pp events is shown in Fig. 11.32. On average, the measured jet energy in Pb–Pb collisions is the same as that in pp. In other words, the background subtraction algorithm gives a reconstructed jet energy which is the same for pp (without background) and for Pb–Pb (with background) interactions.

The jet energy resolution is defined as $\sigma(E_{\mathrm{T}}^{\mathrm{reco}}/E_{\mathrm{T}}^{\mathrm{MC}})/\langle E_{\mathrm{T}}^{\mathrm{reco}}/E_{\mathrm{T}}^{\mathrm{MC}}\rangle$, where $E_{\mathrm{T}}^{\mathrm{reco}}$ and $E_{\mathrm{T}}^{\mathrm{MC}}$ are the reconstructed and generated jet transverse energies. Figure 11.33 shows the jet resolution as a function of $E_{\mathrm{T}}^{\mathrm{MC}}$. The jet energy resolution is degraded by approximatley 20% in high multiplicity central Pb–Pb collisions compared to pp.

Since the azimuthal angle and the rapidity distributions of jets is of particular interest for jet quenching observables in heavy ion collisions, spatial resolution is important. For 100 GeV jets, the η and φ resolutions are 0.028 and 0.032 correspondingly.

The subtraction procedure allows the identification and measurement of jets in heavy ion collisions using only CMS calorimeters with very high efficiency and purity. Jets reconstructed in central Pb–Pb collisions with $E_T > 30$ GeV, that are within $\Delta R < 0.25$ around the direction of the generated MC jet are considered as true QCD jets. The efficiency of jet reconstruction in central Pb–Pb collisions is estimated as the fraction of events with such true QCD jets among all the generated events. The efficiency of finding a true QCD jet is nearly 100% for $E_T = 75(100)$ GeV jets in the barrel (endcap) region.

The purity of the reconstructed jet sample is defined as the number of events with true QCD jets divided by the number of events with at least one reconstructed jet (fake or real) with transverse energy above 30 GeV. Beyond E_{T} = 50 GeV (75 GeV) jets, the purity is nearly 100% for the barrel (endcap).

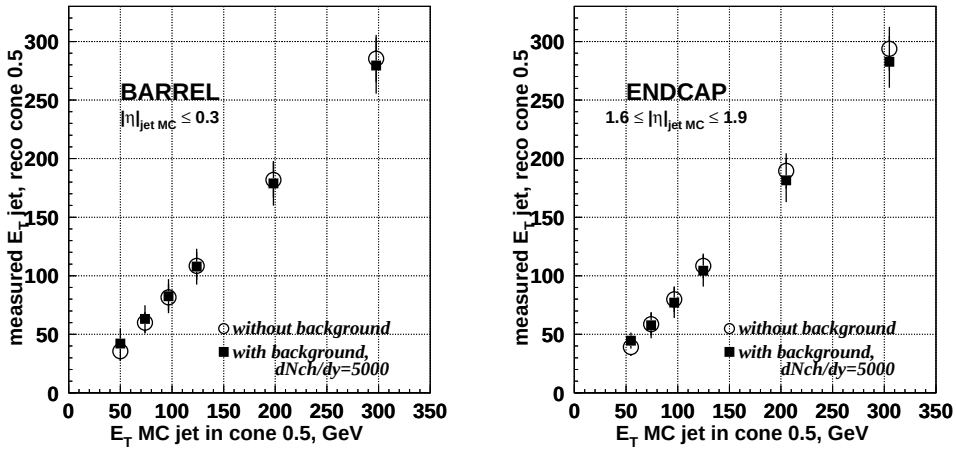

Figure 11.32: The correlation between the average reconstructed and the generated jet transverse energies in Pb–Pb (full squares) and *pp* (open circles) events in the barrel (left) and endcap (right). The error bars are the dispersion of jet energy distribution.

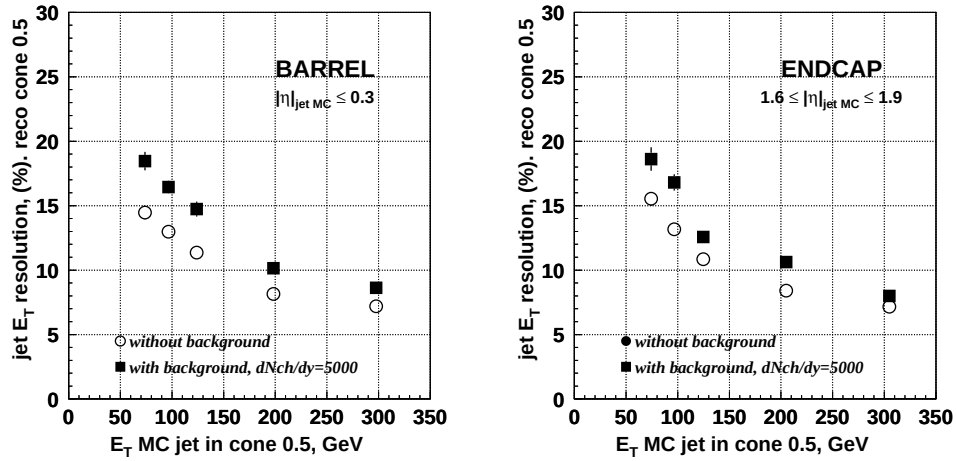

Figure 11.33: Jet energy resolution in Pb–Pb (full squares) and *pp* (open circles) events in the barrel (left) and endcap (right) regions.